https://doi.org/10.5194/egusphere-2026-3894
Preprint. Discussion started: 28 July 2026

Transient simulation of Holocene climatic and isotopic variations across global monsoon regions

Xiaoxu Shi[1,2], Xiya Liu[1], Jiping Liu[1], Martin Werner[2], Hu Yang[1], Francisco W. Cruz[3], Chaoyuan Yang[1], and Gerrit Lohmann[2]

[1]School of Atmospheric Sciences, Sun Yat-Sen University and Southern Marine Science and Engineering Guangdong Laboratory (Zhuhai), Zhuhai, China
[2]Alfred Wegener Institute, Helmholtz Center for Polar and Marine Research, Bremerhaven, Germany
[3]Institute of Geosciences, Sao Paulo University, São Paulo, Brazil

Correspondence: Xiaoxu Shi (xshi@awi.de; shixiaoxu@sml-zhuhai.cn)

Abstract. Speleothem oxygen isotopes provide key insights into Holocene monsoon variability, but the scale-dependent and regionally variable controls on precipitation δ^{18}O remain poorly resolved. Here, we use a continuous 8.3 ka isotope-enabled transient simulation based on AWI-ESM2-wiso to investigate Holocene climatic and isotopic changes and quantify driving mechanisms for the isotopic variations via a four-predictor multiple linear regression (MLR) model. The simulation successfully reproduces the orbitally driven long-term weakening of Northern Hemisphere monsoons and the bipolar hydroclimatic response to the 8.2 ka freshwater perturbation, characterized by a southward Intertropical Convergence Zone (ITCZ) shift, Northern Hemisphere drying and isotopic enrichment, and Southern Hemisphere moistening and depletion. MLR results show that regional precipitation amount serves as the dominant and temporally stable control on monsoon δ^{18}O. Secondary predictors including moisture transport, continental recycling, and source temperature exert regionally divergent and time-varying influences. Supplementary large-scale climate indices can improve model performance for specific monsoon domains. El Niño und die Southern Oscillation (ENSO) is the most widespread teleconnection affecting most monsoon domains, while Atlantic Meridional Overturning Circulation (AMOC) and South Atlantic Convergence Zone (SACZ) act as additional key controls over Southwestern South American Monsoon. Spatial correlation analyses further demonstrate that the precipitation amount effect is weak and spatially heterogeneous at local grid scales but becomes robust and uniform at the regional scale. This further indicates that individual speleothem records may misrepresent large-scale monsoon signals due to local spatial noise, while regional proxy ensembles effectively capture the dominant precipitation-isotope relationship.

1 Introduction

The stable isotopic composition of precipitation, expressed as the ratio of heavy to light oxygen (δ^{18}O) or hydrogen (δD) relative to the Vienna Standard Mean Ocean Water standard, encodes a comprehensive fingerprint of the hydrological cycle (Dansgaard, 1964; Gat, 1996). Isotopic fractionation occurs at every phase transition of water. The lighter isotopologue evaporates preferentially from ocean surfaces, heavy isotopes are progressively removed during atmospheric transport through Rayleigh distillation, and partial re-evaporation of falling precipitation further modifies the isotopic ratio reaching the surface

https://doi.org/10.5194/egusphere-2026-3894
Preprint. Discussion started: 28 July 2026

(Craig, 1961; Galewsky et al., 2016). Because these processes are governed by temperature, humidity, atmospheric circulation, and moisture pathway geometry, δ^{18}O in precipitation ($\delta^{18}O_{\text{precip}}$) integrates information about conditions at the moisture source, along the transport trajectory, and at the deposition site simultaneously (Gat, 1996; Merlivat and Jouzel, 1979). This multi-pathway sensitivity is the key interpretive challenge to using water isotopes as paleoclimate proxies, and separating these contributions requires independent constraints or physically explicit modelling (Galewsky et al., 2016; Jouzel et al., 1997).

Stable water isotopes are preserved in a wide range of natural archives, including ice cores, speleothems, tree-ring cellulose, lake sediment carbonates, and coral aragonite (Lachniet, 2009; Galewsky et al., 2016; Comas-Bru et al., 2020; Jonkers et al., 2026). These archives provide near-continuous isotopic records that serve as the empirical basis for evaluating isotope-enabled climate model simulations and interpreting past hydroclimate variability. As a prominent proxy within this suite of archives, speleothem δ^{18}O has been widely applied to reconstruct Holocene variability over tropical and subtropical monsoon regions (Lachniet, 2009; Comas-Bru et al., 2020). Across the Indian Summer Monsoon domain, speleothem from Oman and Yemen document a progressive increase in δ^{18}O from the early Holocene toward the present, broadly tracking the decline in boreal summer insolation under orbital precession (Fleitmann et al., 2003, 2007; Tian et al., 2023). Analogous trends appear in East Asian cave records (Dykoski et al., 2005), in South American speleothems from Botuverá Cave (Bernal et al., 2016), and across other monsoon regions, demonstrating a globally coherent hydrological response to insolation forcing (Cheng et al., 2012; Wanner et al., 2008).

Despite this broad coherence, the quantitative interpretation of speleothem δ^{18}O remains actively debated. The amount effect, whereby heavier rainfall produces isotopically lighter precipitation (Dansgaard, 1964), provides one widely-known explanation for Holocene trends. However, observational and modelling studies have shown that changes in moisture source temperature, reorganisation of large-scale atmospheric circulation and the ITCZ, and variations in continental moisture recycling can also produce δ^{18}O anomalies of comparable magnitude (Gat, 1996; Tharammal et al., 2021; Zhang et al., 2025). The relative importance of these factors is not uniform across monsoon systems, because each region draws moisture from distinct oceanic sources and responds to orbital forcing through its own dynamical pathway (Cheng et al., 2012; Tharammal et al., 2026). Some studies further demonstrated that upstream changes in moisture origin, rather than local rainfall, can dominate the speleothem signal in the East Asian monsoon domain (Liu et al., 2014a; Battisti et al., 2014; Pausata et al., 2011), whereas Indian Ocean source temperature and transport pathways play a proportionally larger role in records influenced by Arabian Sea moisture (Fleitmann et al., 2007; Tharammal et al., 2026). These drivers shift across the Holocene as background climate evolves under orbital forcing.

Isotope-enabled general circulation models have become the primary tool for bridging the interpretive gap between proxy records and climate system, because they simulate the full physical and isotopic water cycle simultaneously under known boundary conditions (Risi et al., 2010; Werner et al., 2011; Cauquoin et al., 2019). In the monsoon context, Parker et al. (2021) performed a benchmark multi-linear regression (MLR) analysis using GISS ModelE-R output from 8 time-slice simulations covering the Holocene across 7 global monsoon regions, demonstrating that seasonal precipitation amount, moisture source temperature, atmospheric circulation, and continental recycling together explain a substantial fraction of regional δ^{18}O variance, and that the relative importance of each driver differs markedly among regions. A comparable analysis shows that

https://doi.org/10.5194/egusphere-2026-3894
Preprint. Discussion started: 28 July 2026

Holocene Asian monsoon δ^{18}O patterns cannot be explained by a single dominant mechanism (e.g., LeGrande and Schmidt, 2009; Caley et al., 2014). These analysis have established the physical framework within which monsoon δ^{18}O variability can be interpreted, and a logical next step is to test whether the inter-regional contrasts and driver hierarchy diagnosed at time slices remain valid under continuously evolving boundary forcings. Transient simulations with isotope-enabled climate models are therefore helpful to address this question, while multi-model comparisons can further assess the robustness of the identified mechanisms.

A newly-developed isotope-enabled climate model AWI-ESM2-wiso has been validated against mid-Holocene and pre-industrial isotopic observations, and reproduces observed $\delta^{18}O_{\rm precip}$patterns at monsoon sites well enough to support mechanistic analysis (Shi et al., 2023). Here we performed a fully continuous isotope-enabled transient simulation of the Holocene using this model, spanning from 8.3 ka to pre-industrial under time-evolving orbital forcing, greenhouse gas concentrations, freshwater pertubation, and ice-sheet geometry. Across seven major global monsoon regions, we apply a region-specific MLR framework to quantify the time-varying contributions of local precipitation amount, moisture source temperature, atmospheric circulation, and continental recycling to Holocene $\delta^{18}O_{\rm precip}$ variability, following Parker et al. (2021) while based on a continuous run.

The remainder of the paper is organised as follows. Section 2 describes the model, the experimental design, and the statistical framework. Section 3 presents the results. We discuss and conclude in Section 4.

2 Methods

2.1 Model description

This study uses AWIESM2-wiso, the isotope-enabled configuration of the AWI Earth System Model described by Shi et al. (2023). The atmospheric component is ECHAM6-wiso, in which stable water isotope diagnostics (Cauquoin and Werner, 2021) are coupled into the ECHAM6 general circulation model (Stevens et al., 2013). The land surface is represented by JSBACH, which provides the lower boundary condition for the atmosphere and resolves the exchanges of water, energy, momentum, and vegetation between the land and the lower troposphere (Raddatz et al., 2007). The sea ice and ocean are simulated by FESOM2, whose finite-volume dynamical core is formulated on a multi-resolution unstructured grid (Danilov et al., 2017).

The atmosphere is run on the T63L47 grid, corresponding to a global-mean horizontal resolution of approximately 1.9° across 47 vertical levels. The ocean resolution is spatially varying, being about 100 km in the open ocean, 35 km along the equator and the coastlines, and 25 km in the polar oceans, and the vertical is discretised on 46 unevenly spaced levels.

2.2 Experimental design

The transient simulation analysed here is integrated for 8,300 model years, covering the period from 8.3 ka to pre-industrial (PI) under continuously evolving boundary conditions, with stable water isotopes and dynamic vegetation switched on. The simulation is initialised from an 8.3 ka equilibrium time-slice state, and its final model year corresponds to 1950 CE. Orbital

https://doi.org/10.5194/egusphere-2026-3894
Preprint. Discussion started: 28 July 2026

Table 1. Definition of the seven monsoon study regions, including geographic boundaries and the season used to compute seasonal means. NH: Northern Hemisphere summer (MJJAS); SH: Southern Hemisphere summer (NDJFM). Region boundaries follow Parker et al. (2021).

Abbreviation	Region	Longitude	Latitude	Season
ISM	Indian Summer Monsoon	50–95°E	11–32°N	MJJAS
EAM	East Asian Monsoon	100–125°E	20–39°N	MJJAS
IAM	Indo-Australian Monsoon	95–135°E	24°S–5°N	NDJFM
SW-SAM	SW South American Monsoon	80–64°W 68–40°W	10°S–0° 30–10°S	NDJFM
NE-SAM	NE South American Monsoon	300–330°E	10°S–0°	NDJFM
CAM	Central American Monsoon	245–302°E	10–33°N	MJJAS
SAfM	Southern African Monsoon	10–40°E	30–17°S	NDJFM

parameters are computed following Berger (1978), atmospheric greenhouse gas concentrations are derived from the polar ice-core composite of Köhler et al. (2017), and ice-sheet extent and topography are prescribed according to the GLAC-1D reconstruction (Tarasov et al., 2012; Briggs et al., 2014).

The 8.2 ka event is imposed as a two-stage freshwater forcing applied to the Labrador Sea. During the first model year a 2.5 Sv freshwater pulse is released, mimicking the catastrophic outburst of the proglacial Lakes Agassiz and Ojibway through the Hudson Strait (Barber et al., 1999; LeGrande and Schmidt, 2008). This pulse is followed by a sustained background flux of 0.13 Sv prescribed over the subsequent 99 years, representing the rerouting of western Canadian continental runoff into the Labrador Sea after the collapse of the Hudson Bay ice saddle (Carlson et al., 2008).

The PI reference climatology is computed as the mean over the last 500 model years of the simulation (0–500 yr BP), and all anomalies presented hereafter are expressed relative to this baseline.

2.3 Study regions

We define seven global monsoon regions following Parker et al. (2021), summarised in Table 1. Northern Hemisphere (NH) monsoon regions use the boreal summer season May–September (MJJAS); Southern Hemisphere (SH) monsoon regions use the austral summer season November–March (NDJFM).

Each monsoon region is associated with two spatial domains. The precipitation region comprises land-only grid cells within the geographic bounds listed in Table 1; this is where the response variable $\delta^{18}O_{precip}$ is evaluated. The source region comprises ocean-only grid cells in a defined upstream moisture-origin area for each monsoon system, from which sea surface temperature, evaporation, and moisture-flux predictors are extracted.

https://doi.org/10.5194/egusphere-2026-3894
Preprint. Discussion started: 28 July 2026

2.4 Multi-linear regression framework

The response variable for each monsoon region and each annual time step is the area-weighted, precipitation-weighted mean isotope ratio of precipitation, $\delta^{18}\mathrm{O}_{\mathrm{precip}}$, computed as

$$\delta^{18}\mathrm{O}_{\mathrm{precip}} = \frac{\sum_i P_i\, \delta^{18}\mathrm{O}_i\, A_i}{\sum_i P_i\, A_i}, \tag{1}$$

where P_i is the seasonal mean precipitation rate (mm day^{-1}), $\delta^{18}\mathrm{O}_i$ is the isotope ratio (‰) at grid cell i, and A_i is the grid-cell area (m^2). The summation extends over all land grid cells within the monsoon precipitation region, and all quantities are expressed as anomalies relative to the PI mean prior to regression.

Four fixed predictors are included in every regional model. (1) `region_ppt`, the seasonal mean precipitation anomaly (mm day^{-1}) over the monsoon land region; (2) `wind_dir`, the surface wind direction anomaly (°) at the moisture source region, obtained from $\arctan(v/u)$ using the zonal and meridional wind components. This term is a proxy for large-scale atmospheric circulation and moisture transport pathways. (3) `source_temp`, the surface temperature anomaly (°C) at the moisture source region; and (4) `ppt_rec`, the precipitation recycling index anomaly, defined as

$$\mathrm{RI} = \frac{E}{E + 2F_{\mathrm{in}}}, \tag{2}$$

where E is the area-integrated regional evaporation (mm day^{-1}) and F_{in} is the column-integrated moisture influx across the regional boundaries (mm day^{-1}), following Brubaker et al. (1993). The column-integrated moisture flux **F** is computed as

$$F = \frac{1}{g} \sum_k q_k\, u_k\, |\Delta p_k|, \tag{3}$$

where g is gravitational acceleration, q_k and u_k are the specific humidity and wind speed at pressure level k, and Δp_k is the layer thickness. The summation spans all pressure levels from 100,000 Pa near the surface to 1,000 Pa in the upper troposphere.

All climatic and isotopic variables spanning the full 8300-year simulation period were binned into non-overlapping 100-year intervals. A mean value was calculated for each bin, yielding a total of 83 discrete time points. The MLR analysis was then performed based on this processed dataset.

We added 4 annually resolved climate indices (relative to the pre-industrial mean of the final 500 simulation years) to the basic predictors, to capture signals missing from the original MLR framework. These climate indices include the Atlantic Meridional Overturning Circulation (AMOC), Niño 3.4, Southern Annular Mode (SAM) and Arctic Oscillation (AO). The AMOC is the maximum of the meridional overturning streamfunction around 30°N between 500 and 2000 m depth. The Niño 3.4 index is the area-weighted annual-mean sea surface temperature anomaly over the tropical Pacific box 5°S–5°N, 170°W–120°W. The SAM index follows the Marshall (2003) definition as the difference of zonal-mean sea-level pressure

https://doi.org/10.5194/egusphere-2026-3894
Preprint. Discussion started: 28 July 2026

between 40°S and 65°S. The AO is defined as the leading EOF of sea level pressure north of 20°N, with positive values corresponding to reduced Arctic pressure. One additional austral summer (NDJFM) index for the strength of South Atlantic Convergence Zone (SACZ) was calculated as the area-weighted seasonal-mean outgoing longwave radiation (OLR) anomaly within the climatological SACZ band. All indices were processed using the same 100-year binning. We performed forward stepwise selection over all index combinations for each monsoon region. A candidate index was kept only when it raised R^2 by at least 0.02, and no more than 3 extra indices were included per region to prevent overfitting.

3 Results

3.1 Model validation

The large-scale climatology simulated by AWI-ESM has been comprehensively evaluated against observational and reanalysis products in Sidorenko et al. (2019), and the isotope-enabled configuration used here was validated in Shi et al. (2023); we therefore confine the present assessment to a brief assessment of the PI mean state most directly relevant to this study.

The simulated temperature and precipitation fields (Fig. 1) reproduce the principal features of the observed seasonal climatology, including the meridional temperature gradient, the monsoon rainfall maxima over South and Southeast Asia and tropical Africa during MJJAS, and their Southern Hemisphere counterparts during NDJFM. The spatial distribution of $\delta^{18}O_{\mathrm{precip}}$ likewise reflects the well-known continental and altitude effects, with strongly depleted values over the polar ice sheets and progressively enriched values toward the subtropics.

To compare the model against temerature reconstructions, we followed the site-stack methodology of Liu et al. (2014b). We interpolated the model temperature to the 73 proxy locations of Marcott et al. (2013) by bilinear interpolation. For the seasonally biased site-stack, we extracted model values for each location following the seasonal definitions from the original study. Figure 2 presents the transient surface temperature evolution across the globe and three latitudinal bands. Both the model area mean and the annual site-stack exhibit warming toward the present in all bands. The seasonally biased stack, however, yields markedly different behavior. Over the Northern Hemisphere extratropics, the warming signal is reversed into a cooling of approximately 0.5°C from the early to the late Holocene, consistent with the decline in boreal summer insolation that most proxy records in this region preferentially capture. In the tropics and the Southern Hemisphere extratropics, the seasonal bias exerts a comparatively weak influence.

The model-observation on $\delta^{18}O_{\mathrm{precip}}$ (Fig. 3a,b) confirms good agreement between simulated and observed annual mean $\delta^{18}O_{\mathrm{precip}}$ across the full range of proxy values for present-day, lending confidence in the model's capacity to represent isotope fractionation realistically. To further evaluate the model's ability to reproduce Holocene isotopic variability, we compare AWI-ESM-wiso simulated precipitation-weighted $\delta^{18}O$ against speleothem records from the SISALv2 database, restricting the analysis to entities with continuous coverage spanning 8000 BP to present. Applying this criterion, only four monsoon regions yield sufficient records, namely EAM, IAM, SW-SAM, and CAM; speleothem archives from other monsoon regions do not meet the continuity requirement and are therefore excluded. To facilitate direct comparison, the model output, originally referenced to Vienna Standard Mean Ocean Water (VSMOW), was converted to the Vienna Pee Dee Belemnite (VPDB)

https://doi.org/10.5194/egusphere-2026-3894
Preprint. Discussion started: 28 July 2026

scale following the standard linear transformation of Coplen (1988), consistent with the reporting convention of the SISALv2 speleothem records.

The simulated δ^{18}O evolution broadly agrees with the speleothem record across monsoon regions in terms of sign and long-term temporal structure, though with some regional differences in amplitude (Fig. 3c–f). In EAM, the model captures the progressive enrichment from an early-Holocene minimum toward PI values, consistent with the orbitally driven weakening of the East Asian summer monsoon, albeit with a smaller amplitude relative to the observations. In IAM, the model and observations are in close agreement from 6 ka onward, reproducing both the positive trend and magnitude; the main discrepancy lies in the early period from 8 to 6 ka, where the observed depletion is more pronounced than the model suggests. In SW-SAM, the two datasets share the same sign of anomaly throughout the Holocene, with a declining trend from early-Holocene to PI, though again the model amplitude remains somewhat smaller than observed. In CAM, only a single speleothem record is available for comparison, which limits the strength of any quantitative assessment; nevertheless, the overall trend and amplitude are broadly reproduced, with the primary difference being the substantially larger variability present in the proxy record relative to the model output.

3.2 The 8.2 ka event

The simulated climate response to the 8.2 ka freshwater hosing experiment captures the fingerprint of a weakened AMOC, broadly consistent with proxy reconstructions and previous modelling studies (LeGrande et al., 2006; Morrill et al., 2013; Matero et al., 2017). Surface temperature anomalies are strongly negative over the North Atlantic and northwestern Europe, where the suppression of poleward oceanic heat transport drives cooling exceeding 4 K (Fig. 4a), while a modest warming emerges across South Atlantic, reflecting the bipolar seesaw response characteristic of AMOC perturbations (Broecker, 1998; Stouffer et al., 2006). The precipitation response shows a southward displacement of the ITCZ (Fig. 4b), driven by reduced cross-equatorial energy transport (Schneider et al., 2014). Rainfall decreases broadly across the Northern Hemisphere tropics, particularly over the African and Asian monsoon domains, while compensating moistening appears along the Southern Hemisphere convergence zones (Dixit and Kumari, 2026). This interhemispheric precipitation dipole is mirrored in the precipitation-weighted δ^{18}O anomaly field, where enriched values pervade Northern Hemisphere monsoon regions in response to reduced convective rainfall, while isotopically depleted anomalies develop over the southern tropics where precipitation increases and over North Atlantic (Fig. 4c), consistent with the amount effect and the temperature-driven isotopic response documented for the 8.2 ka event (Parker and Harrison, 2022; Lachniet et al., 2004).

3.3 Holocene climate trend

Global maps of linear trends in seasonal surface temperature, precipitation, and $\delta^{18}O_{precip}$ computed over the full 8,300–0 yr BP transient simulation are shown in Fig. 5, with the PI mean as the anomaly reference (Fig. 1). Distinct seasonal asymmetries are apparent in the temperature trends. During boreal summer (MJJAS), cooling dominates most Northern Hemisphere land regions, reflecting the reduction in Northern Hemisphere summer insolation. The Southern Hemisphere exhibits weak warming trends especially over oceans, consistent with the anti-phased insolation response between hemispheres. A no-

https://doi.org/10.5194/egusphere-2026-3894
Preprint. Discussion started: 28 July 2026

table boreal winter (NDJFM) warming trend occurs in both hemispheres as insolation increases, with a stronger signal in the Northern Hemisphere.

Seasonal precipitation trends closely mirror this insolation-driven thermal changes, modulated by ITCZ migration and monsoon circulation shifts (Fleitmann et al., 2007; Braconnot et al., 2007b, a). In MJJAS, pronounced drying over the tropical Africa, South Asia, and East Asia reflects the weakening of NH summer monsoons as boreal summer insolation declined, while compensating moistening appears along Southern Hemisphere convergence zones. The NDJFM pattern exhibits broadly opposite tendencies, with drying in the Southern Hemisphere tropics and relative moistening in NH low latitudes, indicating the cross-equatorial energy transport adjustments associated with the evolving latitudinal insolation gradient (Schneider et al., 2014). The precipitation-weighted δ^{18}O trends largely follow these hydroclimate changes but also reflect upstream thermodynamic effects (Liu et al., 2014a; Battisti et al., 2014; Pausata et al., 2011); enrichment (depletion) of δ^{18}O over monsoon-influenced regions during MJJAS (NDJFM) is consistent with a reduction (enhancement) in convective rainfall and moisture recycling.

3.4 Multiple linear regression analysis

3.4.1 Pooled regression and the dominance of the amount effect

We applied the four-predictor MLR framework described in Sect. 2.4 to the simulated δ^{18}O for the predefined seven monsoon domains (Fig. 6a). As shown in Fig. 6b–e, the pooled regression captures 62.9 % of total precipitation δ^{18}O variance across all samples. Summer precipitation anomaly produces the steepest negative regression slope, which confirms the amount effect acts as a consistent dominant control across all monsoon regions. The remaining three predictors show statistical significance for the full pooled dataset but feature pronounced regional heterogeneity in their statistical robustness and regression slopes. Wind direction holds positive slopes for all regions, but scattered points for ISM and SAfM depart strongly from the regression line and display insignificant local correlations. Precipitation recycling produces a positive slope for most regions, whereas NE-SAM and CAM data spread widely away from the regression line without detectable significant local dependence. For source-region temperature, we observe a pooled positive slope, but certain regions (EAM, CAM) exhibit heavily dispersed residuals and non-significant regression slopes.

The pooled simulated-versus-predicted scatter (Fig. 6f) anchors these regression statistics to the simulated anomaly distribution. EAM data generally clusters relatively close to the 1:1 reference line and shows comparatively favorable fitting among all seven regions. By contrast, ISM points scatter widely away from the reference line, indicating the four-predictor MLR framework cannot fully reproduce observed ISM δ^{18}O variability and leaves substantial unexplained regional residual variance. Points from IAM, CAM and SW-SAM systematically shift toward positive predicted values relative to observed values, meaning the regression tends to overestimate precipitation δ^{18}O magnitude for these three monsoon systems. NE-SAM and SAfM show moderate dispersion and stay comparatively close to the reference line with limited bias. The centennial-scale fits track the full simulated δ^{18}O history, with a skill that varies by region (Fig. 7). EAM presents the most reliable reproduction of δ^{18}O evolution with the highest R^2 of 0.963. NE-SAM, CAM and IAM also achieve strong model performance, with their R^2

https://doi.org/10.5194/egusphere-2026-3894
Preprint. Discussion started: 28 July 2026

being 0.80, 0.74 and 0,654, respectively. By contrast, SW-SAM presents notably poor fitting ($R^2 = 0.295$). The MLR-derived time series appears excessively smoothed and fails to reproduce the large-amplitude short-term oscillations seen in observed data, meaning the model substantially underestimates the real magnitude of local isotopic variability for this region.

Figure 8 documents centennial-scale temporal evolution of four regression coefficients throughout the Holocene, based on sliding-window MLR to quantify time-dependent modulation strength of each predictor toward precipitation δ^{18}O. Local precipitation maintains consistently negative coefficients across all time periods and all monsoon domains, with the full-Holocene average value at -0.749 ± 0.381 ‰ (mm day^{-1})$^{-1}$. The stable negative sign further confirms the persistent amount effect across orbital and centennial timescales, even though regional coefficient magnitudes fluctuate gradually over millennia. Wind direction and source-region temperature feature near-zero long-term mean coefficients at $+0.001 \pm 0.054$ and -0.011 ± 0.585 ‰ (mm day^{-1})$^{-1}$ respectively, with substantial multi-millennial swings of regional slopes crossing positive and negative values. The recycling coefficient show a weakly positive full-record average and has the largest inter-region spread ($+0.113 \pm 3.565$ ‰ (mm day^{-1})$^{-1}$), with NE-SAM showing a pronounced negative slope from 6 ka onward.

3.4.2 Contribution from climate indices

As above, the four baseline predictors (precipitation amount, wind direction, recycling ratio, and source temperature) explain a wide range of the regional δ^{18}O variance across the seven monsoon domains, with R^2 values varying substantially. For instance, the East Asian Monsoon (EAM) shows the highest explanatory power, with a baseline R^2 of 0.963, while the Southwestern South American Monsoon (SW-SAM) displays the lowest baseline performance, at only 0.295.

Adding climate indices to the baseline MLR framework produces regionally heterogeneous gains in explained variance, as shown in Fig. 9. For regions already well captured by the four-predictor model, such as the NE-SAM (baseline $R^2 = 0.80$) and CAM ($R^2 = 0.74$), none of the tested climate indices deliver a meaningful rise in R^2. By contrast, climate indices do provide meaningful additional explanatory power for several other monsoon regions. The Niño 3.4 index emerges as the most widely useful supplementary predictor, selected for the ISM, SW-SAM, and SAfM. For ISM, adding the detrended Niño 3.4 index increases the R^2 by 0.138, raising the total explained variance to 0.595. For SW-SAM, the Niño 3.4 index is the first selected predictor, contributing an R^2 gain of 0.209, followed by small improvements from AMOC ($\Delta R^2 = 0.025$) and SACZ strength ($\Delta R^2 = 0.026$), bringing the final R^2 to 0.555. SAfM also benefits from the Niño 3.4 index, with a modest R^2 increase of 0.089. For the IAM, SAM and AMOC are selected instead, with combined gains of 0.059 and a final R^2 of 0.712.

Overall, the results indicate that the four baseline predictors are sufficient to capture most δ^{18}O variability in most monsoon regions, while ENSO (represented by the Niño 3.4 index) and, to a lesser extent, AMOC and SACZ-related processes provide additional, region-specific controls that are not fully captured by the baseline variables.

3.4.3 The amount effect is a regional-scale relationship

Our preceding MLR analyses highlight precipitation amount as the dominant control on precipitation δ^{18}O at "regional" scale. The amount effect is often stated as a "local" relation between in-situ rainfall and precipitation δ^{18}O, which motivates us to examine how this correlation behaves across contrasting spatial resolutions here (Fig. 10). At the local level, the correlation

https://doi.org/10.5194/egusphere-2026-3894
Preprint. Discussion started: 28 July 2026

between grid-cell δ^{18}O and precipitation inside the monsoon boxes is moderately negative in most cells but patchy (Fig. 10a), with certain areas of weak or near-zero correlation, particularly over parts of ISM and CAM domains. Replacing local grid precipitation with region-averaged precipitation only leads to scattered regional shifts, as some grid cells develop stronger negative correlation (darker blue shading) while others show weakened relationship (lighter color), without systematic intensification (Fig. 10b). In stark contrast, region-averaged data in Fig. 10c produce uniformly stronger negative correlations.

Our scale-dependent correlation results bear concrete implications for proxy interpretation. A single speleothem, precipitated within a grid cell of weak local amount effect, cannot faithfully capture regional rainfall signals commonly interpreted from its δ^{18}O record. Instead, composite averaging of multiple speleothems filters out site-specific spatial noise and restores the prominent region-scale amount effect. Such spatial dependence supports an ensemble-based approach to interpret speleothem δ^{18}O records.

4 Discussion and conclusions

A continuous 8,300-year isotope-enabled transient simulation with AWI-ESM2-wiso has allowed us to examine the climate change to slow Holocene orbital and greenhouse gas forcings. The Holocene temperature evolution simulated here, with high-latitude Northern Hemisphere summer cooling, modest Southern Hemisphere warming, and a long progressive weakening of the Northern Hemisphere monsoon systems, fits within the long-running debate about the Holocene Thermal Maximum. The proxy stack of Marcott et al. (2013) and the multi-method synthesis of Kaufman et al. (2020) document a clear mid-Holocene warmth followed by late-Holocene cooling, but data-assimilation reconstructions place the temperature evolution closer to a slow monotonic warming since the early Holocene (Osman et al., 2021), and the proxy signal itself has been argued to reflect a seasonal rather than annual temperature evolution (Bova et al., 2021). Our simulation, like other recent transient runs analyzed in this debate (Kaufman and Broadman, 2023; Cartapanis et al., 2022; Bader et al., 2020), reproduces the model side of the discrepancy and is consistent with the view that the proxy-model offset is largely a seasonal artifact rather than a missing physical forcing. On the monsoon side, the simulated Northern Hemisphere weakening and Southern Hemisphere antiphase response track the long-recognised precession pacing of tropical hydroclimate (Cheng et al., 2016; Fleitmann et al., 2003; Deininger et al., 2020).

The 8.2 ka response in the simulation reproduces the classical fingerprint of a transient AMOC slowdown: deep North Atlantic cooling (Alley et al., 1997), a southward shift of the tropical rainbelt (Schneider et al., 2014), drying across the NH monsoon belt, and isotopically enriched precipitation over Asia coincident with isotopically depleted precipitation over the southern tropics. This pattern matches the global speleothem synthesis of Parker and Harrison (2022), who found systematic positive δ^{18}O anomalies of order $+0.5‰$ across NH cave sites and negative anomalies of comparable magnitude in the Southern Hemisphere, and is corroborated by the high-resolution Heshang Cave reconstruction of Liu et al. (2013) and by Brazilian and Omani records compiled in Cheng et al. (2009). Tropical hydroclimatic responses recorded in the Indo-Pacific warm pool (Dixit et al., 2024) and in northern Spanish speleothems (Kilhavn et al., 2022) provide further geographic anchors against which our hosing experiment can be assessed. The agreement with these recent compilations supports the view that the bipolar

https://doi.org/10.5194/egusphere-2026-3894
Preprint. Discussion started: 28 July 2026

seesaw pattern of monsoonal δ^{18}O during the 8.2 ka event is a robust feature of the freshwater-forced response, which our model captures correctly.

Our MLR work enables a direct comparison with the benchmark time-slice work of Parker et al. (2021), who applied the same four-predictor scheme across eight discrete Holocene snapshots from GISS ModelE-R. Consistent with their core findings, our regression confirms that precipitation amount, source temperature, atmospheric circulation and continental recycling together explain a large fraction of regional δ^{18}O variance, and that the relative weight of each driver differs markedly among regions. Precipitation amount dominates persistent negative coefficients across all timescales and regions, forming the core constraint from the amount effect. By contrast, the three secondary predictors yield positive pooled regression slopes, but with region-dependent coefficient signs and magnitudes.

Nevertheless, notable regional discrepancies exist between our results and Parker et al. (2021). In their analysis, for example, precipitation exerts limited control over δ^{18}O in EAM, NE-SAM and CAM whose data depart strongly from the global regression trend, while precipitation dominates ISM, IAM, SW-SAM and SAfM. By contrast, all seven monsoon domains in our dataset closely follow the global precipitation regression slope, highlighting precipitation as a key driver universally. Source-region wind direction serves as a proxy for large-scale atmospheric circulation and moisture transport pathways; its regression sign reflects shifts in moisture source location and advection distance, thereby modulating precipitation δ^{18}O variability. For this circulation indicator (source-region wind direction), Parker et al. (2021) found EAM, ISM and IAM well correlated with the variance but CAM, SW-SAM, NE-SAM and SAfM deviate considerably; our results instead show wind direction is critical for EAM, SW-SAM and NE-SAM, but plays a negligible role for ISM.

Recycling presents significantly positive coefficients for most monsoon regions in our outputs. Transpired and surface-evaporated moisture returns to the boundary layer (Gat and Matsui, 1991; Winnick et al., 2014), and Risi et al. (2013) confirmed using satellite isotope observations and isotope-enabled simulations that this transpiration-dominated recycling injects an enriched signal into low-level vapour. More inland, the role of continental recycling becomes important. The positive coefficient in our study reflects this enrichment pathway. Regarding source temperature, Bony et al. (2008) decomposed the SST-δ^{18}O relationship into a dynamical pathway, in which SST anomalies covary with large-scale circulation, producing the amount effect through enhanced rainout, and a thermodynamic pathway (SST changes at fixed circulation), in which the temperature dependence of the liquid-vapour fractionation factor produces isotopically heavier evaporated vapour (fractionation factor α falls from 1.0117 at 0°C to 1.0098 at 20°C; Majoube, 1971). The sign and magnitude of the source temperature regression slope across individual monsoon regions are therefore governed by the relative balance between these competing thermodynamic and dynamical controls.

Our Holocene transient run enables rolling-window regression to track temporal shifts in regression coefficients across the Holocene. Precipitation-related coefficients remain stable and transferable across orbital states, whereas wind direction, source temperature and recycling coefficients vary substantially over time and even switch sign in the monsoon regions. A regression calibrated at one orbital configuration therefore does not transfer without correction to another. However, such non-stationarity also likely reflects relatively small changes of individual predictors within each 1000-yr analysis window.

https://doi.org/10.5194/egusphere-2026-3894
Preprint. Discussion started: 28 July 2026

Beyond the four local-process predictors, large-scale climate indices contribute significantly to regional isotope variance in several monsoon domains. The Niño 3.4 index emerges as the most widely useful supplementary predictor across both hemispheres, notably improving model skill for ISM, SW-SAM, and SAfM. This identifies ENSO as the dominant large-scale teleconnection that the local predictor set fails to capture on centennial timescales. In the Southern Hemisphere, our results highlight the importance of SACZ dynamics for SW-SAM variability. Specifically, the SACZ strength index yields a small but significant incremental gain for SW-SAM. Additionally, the inclusion of the AMOC index further improves SW-SAM model performance, consistent with stalagmite reconstructions from southeast Brazil that place SW-SAM hydroclimate firmly under remote North Atlantic forcing on millennial to orbital timescales (Stríkis et al., 2018).

Finally, although our MLR analyses robustly validate the prevalence of the amount effect across monsoon regions, this does not equate to that in-situ isotopic variations at individual sites directly reflect local precipitation changes. The amount effect exhibits substantial spatial heterogeneity at the grid-cell level but becomes universally pronounced when averaged to the regional scale. Accordingly, a single speleothem record may be located within a grid cell where the local rainfall signal is weak, whereas regional composite datasets effectively eliminate spatial noise and recover the dominant amount effect. This mechanism provides a physical explanation for the empirical consensus within the SISAL community that regional speleothem composites better represent large-scale monsoon variability than individual cave records (Comas-Bru et al., 2020; Lachniet, 2009). For paleomonsoon reconstruction, we therefore argue that regional aggregation of speleothem δ^{18}O data is a more reliable quantitative approach than single-site interpretation.

Data availability. The AWI-ESM-2.1-wiso seasonal-mean and monthly model output used in this study (the full 8.3 ka to 0 ka transient including the 100-yr 8.2 ka hosing experiment) is archived at Zenodo, doi:10.5281/zenodo.21068858 (Shi, 2026). The repository contains all NetCDF input fields required to reproduce the multi-linear regression analysis of the seven monsoon regions, together with the raw fields used to derive the climate-mode indices (AMOC, Niño3.4, SAM, AO, OLR-based SACZ).

Author contributions. X.S. designed the study, performed the simulations, conducted the analyses, and wrote the manuscript. All authors contributed to the discussion and writing of the manuscript.

Competing interests. The author declares that there are no competing interests.

Acknowledgements. This study is supported by the Southern Marine Science and Engineering Guangdong Laboratory (Zhuhai) (grant no. SML2023SP204) and the Guangdong Basic and Applied Basic Research Foundation (grant no. 2025A1515012165). The authors gratefully acknowledge the computing resources provided by the German Climate Computing Center (DKRZ) in Hamburg (project: ba0989).

https://doi.org/10.5194/egusphere-2026-3894
Preprint. Discussion started: 28 July 2026

References

Alley, R. B., Mayewski, P. A., Sowers, T., Stuiver, M., Taylor, K. C., and Clark, P. U.: Holocene climatic instability: A prominent, widespread event 8200 yr ago, Geology, 25, 483–486, 1997.

Bader, J., Jungclaus, J., Krivova, N., Lorenz, S., Maycock, A., Raddatz, T., Schmidt, H., Toohey, M., Wu, C.-J., and Claussen, M.: Global temperature modes shed light on the Holocene temperature conundrum, Nature communications, 11, 4726, 2020.

Barber, D. C., Dyke, A., Hillaire-Marcel, C., Jennings, A. E., Andrews, J. T., Kerwin, M. W., Bilodeau, G., McNeely, R., Southon, J., Morehead, M. D., et al.: Forcing of the cold event of 8,200 years ago by catastrophic drainage of Laurentide lakes, Nature, 400, 344–348, 1999.

Battisti, D., Ding, Q., and Roe, G.: Coherent pan-Asian climatic and isotopic response to orbital forcing of tropical insolation, Journal of Geophysical Research: Atmospheres, 119, 11–997, 2014.

Berger, A. L.: Long-term variations of daily insolation and Quaternary climatic changes, Journal of the Atmospheric Sciences, 35, 2362–2367, https://doi.org/10.1175/1520-0469(1978)035<2362:LTVODI>2.0.CO;2, 1978.

Bernal, J. P., Cruz, F. W., Stríkis, N. M., Wang, X., Deininger, M., Catunda, M. C. A., Ortega-Obregón, C., Cheng, H., Edwards, R. L., and Auler, A. S.: High-resolution Holocene South American monsoon history recorded by a speleothem from Botuverá Cave, Brazil, Earth and Planetary Science Letters, 450, 186–196, 2016.

Bony, S., Risi, C., and Vimeux, F.: Influence of convective processes on the isotopic composition (δ18O and δD) of precipitation and water vapor in the tropics: 1. Radiative-convective equilibrium and Tropical Ocean–Global Atmosphere–Coupled Ocean-Atmosphere Response Experiment (TOGA-COARE) simulations, Journal of Geophysical Research: Atmospheres, 113, 2008.

Bova, S., Rosenthal, Y., Liu, Z., Godad, S. P., and Yan, M.: Seasonal origin of the thermal maxima at the Holocene and the last interglacial, nature, 589, 548–553, 2021.

Braconnot, P., Otto-Bliesner, B., Harrison, S., Joussaume, S., Peterchmitt, J.-Y., Abe-Ouchi, A., Crucifix, M., Driesschaert, E., Fichefet, T., Hewitt, C., et al.: Results of PMIP2 coupled simulations of the Mid-Holocene and Last Glacial Maximum–Part 2: feedbacks with emphasis on the location of the ITCZ and mid-and high latitudes heat budget, Climate of the Past, 3, 279–296, 2007a.

Braconnot, P., Otto-Bliesner, B., Harrison, S., Joussaume, S., Peterchmitt, J.-Y., Abe-Ouchi, A., Crucifix, M., Driesschaert, E., Fichefet, T., Hewitt, C., et al.: Results of PMIP2 coupled simulations of the Mid-Holocene and Last Glacial Maximum–Part 1: experiments and large-scale features, Climate of the Past, 3, 261–277, 2007b.

Briggs, R. D., Pollard, D., and Tarasov, L.: A data-constrained large ensemble analysis of Antarctic evolution since the Eemian, Quaternary Science Reviews, 103, 91–115, https://doi.org/10.1016/j.quascirev.2014.09.003, 2014.

Broecker, W. S.: Paleocean circulation during the last deglaciation: a bipolar seesaw?, Paleoceanography, 13, 119–121, 1998.

Brubaker, K. L., Entekhabi, D., and Eagleson, P. S.: Estimation of Continental Precipitation Recycling, Journal of Climate, 6, 1077–1089, https://doi.org/10.1175/1520-0442(1993)006<1077:EOCPR>2.0.CO;2, 1993.

Caley, T., Roche, D. M., and Renssen, H.: Orbital Asian summer monsoon dynamics revealed using an isotope-enabled global climate model, Nature communications, 5, 5371, 2014.

Carlson, A. E., LeGrande, A. N., Oppo, D. W., Came, R. E., Schmidt, G. A., Anslow, F. S., Licciardi, J. M., and Obbink, E. A.: Rapid early Holocene deglaciation of the Laurentide ice sheet, Nature Geoscience, 1, 620–624, 2008.

Cartapanis, O., Jonkers, L., Moffa-Sanchez, P., Jaccard, S. L., and De Vernal, A.: Complex spatio-temporal structure of the Holocene Thermal Maximum, Nature Communications, 13, 5662, 2022.

Cauquoin, A. and Werner, M.: High-resolution nudged isotope modeling with ECHAM6-wiso: Impacts of updated model physics and ERA5 reanalysis data, Journal of Advances in Modeling Earth Systems, 13, e2021MS002 532, https://doi.org/10.1029/2021MS002532, 2021.

Cauquoin, A., Werner, M., and Lohmann, G.: Water isotopes–climate relationships for the mid-Holocene and preindustrial period simulated with an isotope-enabled version of MPI-ESM, Climate of the Past, 15, 1913–1937, 2019.

Cheng, H., Fleitmann, D., Edwards, R. L., Wang, X., Cruz, F. W., Auler, A. S., Mangini, A., Wang, Y., Kong, X., Burns, S. J., et al.: Timing and structure of the 8.2 kyr BP event inferred from δ18O records of stalagmites from China, Oman, and Brazil, Geology, 37, 1007–1010, 2009.

Cheng, H., Sinha, A., Wang, X., Cruz, F. W., and Edwards, R. L.: The Global Paleomonsoon as seen through speleothem records from Asia and the Americas, Climate dynamics, 39, 1045–1062, 2012.

Cheng, H., Edwards, R. L., Sinha, A., Spötl, C., Yi, L., Chen, S., Kelly, M., Kathayat, G., Wang, X., Li, X., et al.: The Asian monsoon over the past 640,000 years and ice age terminations, nature, 534, 640–646, 2016.

Comas-Bru, L., Rehfeld, K., Roesch, C., Amirnezhad-Mozhdehi, S., Harrison, S. P., Atsawawaranunt, K., Ahmad, S. M., Ait Brahim, Y., Baker, A., Bosomworth, M., et al.: SISALv2: A comprehensive speleothem isotope database with multiple age-depth models, Earth System Science Data Discussions, 2020, 1–47, 2020.

Coplen, T. B.: Normalization of oxygen and hydrogen isotope data, Chemical Geology: Isotope Geoscience Section, 72, 293–297, 1988.

Craig, H.: Isotopic variations in meteoric waters, Science, 133, 1702–1703, 1961.

Danilov, S., Sidorenko, D., Wang, Q., and Jung, T.: The Finite-volumeE Sea ice–Ocean Model (FESOM2), Geoscientific Model Development, 10, 765–789, https://doi.org/10.5194/gmd-10-765-2017, 2017.

Dansgaard, W.: Stable isotopes in precipitation, tellus, 16, 436–468, 1964.

Deininger, M., McDermott, F., Cruz, F. W., Bernal, J. P., Mudelsee, M., Vonhof, H., Millo, C., Spötl, C., Treble, P. C., Pickering, R., et al.: Inter-hemispheric synchroneity of Holocene precipitation anomalies controlled by Earth's latitudinal insolation gradients, Nature communications, 11, 5447, 2020.

Dixit, Y. and Kumari, A.: The 8.2 Ka Abrupt Climate Event: Causes, Impacts and Future Implications, Wiley Interdisciplinary Reviews: Climate Change, 17, e70 050, 2026.

Dixit, Y., Chua, S., Yan, Y. T., Kumari, A., and Switzer, A. D.: Hydroclimatic impacts of the abrupt cooling event 8200 years ago in the western Indo-Pacific Warm Pool, Communications Earth & Environment, 5, 690, 2024.

Dykoski, C. A., Edwards, R. L., Cheng, H., Yuan, D., Cai, Y., Zhang, M., Lin, Y., Qing, J., An, Z., and Revenaugh, J.: A high-resolution, absolute-dated Holocene and deglacial Asian monsoon record from Dongge Cave, China, Earth and Planetary Science Letters, 233, 71–86, 2005.

Fleitmann, D., Burns, S. J., Mudelsee, M., Neff, U., Kramers, J., Mangini, A., and Matter, A.: Holocene forcing of the Indian monsoon recorded in a stalagmite from southern Oman, science, 300, 1737–1739, 2003.

Fleitmann, D., Burns, S. J., Mangini, A., Mudelsee, M., Kramers, J., Villa, I., Neff, U., Al-Subbary, A. A., Buettner, A., Hippler, D., et al.: Holocene ITCZ and Indian monsoon dynamics recorded in stalagmites from Oman and Yemen (Socotra), Quaternary Science Reviews, 26, 170–188, 2007.

Galewsky, J., Steen-Larsen, H. C., Field, R. D., Worden, J., Risi, C., and Schneider, M.: Stable isotopes in atmospheric water vapor and applications to the hydrologic cycle, Reviews of Geophysics, 54, 809–865, 2016.

Gat, J. and Matsui, E.: Atmospheric water balance in the Amazon Basin: an isotopic evapotranspiration model, Journal of Geophysical Research: Atmospheres, 96, 13 179–13 188, 1991.

https://doi.org/10.5194/egusphere-2026-3894
Preprint. Discussion started: 28 July 2026

Gat, J. R.: Oxygen and hydrogen isotopes in the hydrologic cycle, Annual Review of Earth and Planetary Sciences, 24, 225–262, 1996.

Jonkers, L., Hollstein, M., Siccha, M., and Kucera, M.: The PALMOD 130k marine palaeoclimate data synthesis version 2, Earth System Science Data, 18, 3013–3068, 2026.

Jouzel, J., Alley, R., Cuffey, K., Dansgaard, W., Grootes, P., Hoffmann, G., Johnsen, S., Koster, R., Peel, D., Shuman, C., et al.: Validity of the temperature reconstruction from water isotopes in ice cores, Journal of Geophysical Research: Oceans, 102, 26 471–26 487, 1997.

Kaufman, D., McKay, N., Routson, C., Erb, M., Davis, B., Heiri, O., Jaccard, S., Tierney, J., Dätwyler, C., Axford, Y., et al.: A global database of Holocene paleotemperature records, Scientific data, 7, 115, 2020.

Kaufman, D. S. and Broadman, E.: Revisiting the Holocene global temperature conundrum, Nature, 614, 425–435, 2023.

Kilhavn, H., Couchoud, I., Drysdale, R. N., Rossi, C., Hellstrom, J., Arnaud, F., and Wong, H.: The 8.2 ka event in northern Spain: timing, structure and climatic impact from a multi-proxy speleothem record, Climate of the Past, 18, 2321–2344, 2022.

Köhler, P., Nehrbass-Ahles, C., Schmitt, J., Stocker, T. F., and Fischer, H.: A 156 kyr smoothed history of the atmospheric greenhouse gases CO_2, CH_4 and N_2O and their radiative forcing, Earth System Science Data, 9, 363–387, https://doi.org/10.5194/essd-9-363-2017, 2017.

Lachniet, M. S.: Climatic and environmental controls on speleothem oxygen-isotope values, Quaternary Science Reviews, 28, 412–432, 2009.

Lachniet, M. S., Asmerom, Y., Burns, S. J., Patterson, W. P., Polyak, V. J., and Seltzer, G. O.: Tropical response to the 8200 yr BP cold event? Speleothem isotopes indicate a weakened early Holocene monsoon in Costa Rica, Geology, 32, 957–960, 2004.

LeGrande, A. and Schmidt, G.: Sources of Holocene variability of oxygen isotopes in paleoclimate archives, Climate of the Past, 5, 441–455, 2009.

LeGrande, A., Schmidt, G., Shindell, D., Field, C., Miller, R., Koch, D., Faluvegi, G., and Hoffmann, G.: Consistent simulations of multiple proxy responses to an abrupt climate change event, Proceedings of the National Academy of Sciences, 103, 837–842, 2006.

LeGrande, A. N. and Schmidt, G. A.: Ensemble, water isotope–enabled, coupled general circulation modeling insights into the 8.2 ka event, Paleoceanography, 23, 2008.

Liu, Y., Henderson, G., Hu, C., Mason, A., Charnley, N., Johnson, K., and Xie, S.: Links between the East Asian monsoon and North Atlantic climate during the 8,200 year event, Nature Geoscience, 6, 117–120, 2013.

Liu, Z., Wen, X., Brady, E., Otto-Bliesner, B., Yu, G., Lu, H., Cheng, H., Wang, Y., Zheng, W., Ding, Y., et al.: Chinese cave records and the East Asia summer monsoon, Quaternary Science Reviews, 83, 115–128, 2014a.

Liu, Z., Zhu, J., Rosenthal, Y., Zhang, X., Otto-Bliesner, B. L., Timmermann, A., Smith, R. S., Lohmann, G., Zheng, W., and Elison Timm, O.: The Holocene temperature conundrum, Proceedings of the National Academy of Sciences, 111, E3501–E3505, 2014b.

Majoube, M.: Fractionnement en oxygène 18 et en deutérium entre l'eau et sa vapeur, Journal de Chimie Physique, 68, 1423–1436, 1971.

Marcott, S. A., Shakun, J. D., Clark, P. U., and Mix, A. C.: A reconstruction of regional and global temperature for the past 11,300 years, science, 339, 1198–1201, 2013.

Marshall, G. J.: Trends in the Southern Annular Mode from observations and reanalyses, Journal of climate, 16, 4134–4143, 2003.

Matero, I., Gregoire, L., Ivanovic, R., Tindall, J., and Haywood, A.: The 8.2 ka cooling event caused by Laurentide ice saddle collapse, Earth and Planetary Science Letters, 473, 205–214, 2017.

Merlivat, L. and Jouzel, J.: Global climatic interpretation of the deuterium-oxygen 18 relationship for precipitation, Journal of Geophysical Research: Oceans, 84, 5029–5033, 1979.

Morrill, C., LeGrande, A. N., Renssen, H., Bakker, P., and Otto-Bliesner, B. L.: Model sensitivity to North Atlantic freshwater forcing at 8.2 ka, Climate of the Past, 9, 955–968, 2013.

https://doi.org/10.5194/egusphere-2026-3894
Preprint. Discussion started: 28 July 2026

Osman, M. B., Tierney, J. E., Zhu, J., Tardif, R., Hakim, G. J., King, J., and Poulsen, C. J.: Globally resolved surface temperatures since the Last Glacial Maximum, Nature, 599, 239–244, 2021.

Parker, S. E. and Harrison, S. P.: The timing, duration and magnitude of the 8.2 ka event in global speleothem records, Scientific Reports, 12, 10 542, 2022.

Parker, S. E., Harrison, S. P., Comas-Bru, L., Kaushal, N., LeGrande, A. N., and Werner, M.: A data–model approach to interpreting speleothem oxygen isotope records from monsoon regions, Climate of the Past, 17, 1119–1138, 2021.

Pausata, F. S., Battisti, D. S., Nisancioglu, K. H., and Bitz, C. M.: Chinese stalagmite δ18O controlled by changes in the Indian monsoon during a simulated Heinrich event, Nature Geoscience, 4, 474–480, 2011.

Raddatz, T. J., Reick, C. H., Knorr, W., Kattge, J., Roeckner, E., Schnur, R., Schnitzler, K.-G., Wetzel, P., and Jungclaus, J.: Will the tropical land biosphere dominate the climate–carbon cycle feedback during the twenty-first century?, Climate Dynamics, 29, 565–574, https://doi.org/10.1007/s00382-007-0247-8, 2007.

Risi, C., Bony, S., Vimeux, F., and Jouzel, J.: Water-stable isotopes in the LMDZ4 general circulation model: Model evaluation for present-day and past climates and applications to climatic interpretations of tropical isotopic records, Journal of Geophysical Research: Atmospheres, 115, 2010.

Risi, C., Noone, D., Frankenberg, C., and Worden, J.: Role of continental recycling in intraseasonal variations of continental moisture as deduced from model simulations and water vapor isotopic measurements, Water Resources Research, 49, 4136–4156, 2013.

Schneider, T., Bischoff, T., and Haug, G. H.: Migrations and dynamics of the intertropical convergence zone, nature, 513, 45–53, 2014.

Shi, X.: AWI-ESM-2.1-wiso Holocene transient simulation: seasonal-mean output for MLR analysis of monsoon δ^{18}O, https://doi.org/10.5281/zenodo.21068859, 2026.

Shi, X., Cauquoin, A., Lohmann, G., Jonkers, L., Wang, Q., Yang, H., Sun, Y., and Werner, M.: Simulated stable water isotopes during the mid-Holocene and pre-industrial periods using AWI-ESM-2.1-wiso, Geoscientific Model Development, 16, 5153–5178, 2023.

Sidorenko, D., Goessling, H., Koldunov, N., Scholz, P., Danilov, S., Barbi, D., Cabos, W., Gurses, O., Harig, S., Hinrichs, C., et al.: Evaluation of FESOM2. 0 coupled to ECHAM6. 3: preindustrial and HighResMIP simulations, Journal of Advances in Modeling Earth Systems, 11, 3794–3815, 2019.

Stevens, B., Giorgetta, M., Esch, M., Mauritsen, T., Crueger, T., Rast, S., Salzmann, M., Schmidt, H., Bader, J., Block, K., Brokopf, R., Fast, I., Kinne, S., Kornblueh, L., Lohmann, U., Pincus, R., Reichler, T., and Roeckner, E.: Atmospheric component of the MPI-M Earth System Model: ECHAM6, Journal of Advances in Modeling Earth Systems, 5, 146–172, https://doi.org/10.1002/jame.20015, 2013.

Stouffer, R. J., Yin, J.-j., Gregory, J., Dixon, K., Spelman, M., Hurlin, W., Weaver, A., Eby, M., Flato, G., Hasumi, H., et al.: Investigating the causes of the response of the thermohaline circulation to past and future climate changes, Journal of climate, 19, 1365–1387, 2006.

Stríkis, N. M., Cruz, F. W., Barreto, E. A., Naughton, F., Vuille, M., Cheng, H., Voelker, A. H., Zhang, H., Karmann, I., Edwards, R. L., et al.: South American monsoon response to iceberg discharge in the North Atlantic, Proceedings of the National Academy of Sciences, 115, 3788–3793, 2018.

Tarasov, L., Dyke, A. S., Neal, R. M., and Peltier, W. R.: A data-calibrated distribution of deglacial chronologies for the North American ice complex from glaciological modeling, Earth and Planetary Science Letters, 315–316, 30–40, https://doi.org/10.1016/j.epsl.2011.09.010, 2012.

Tharammal, T., Bala, G., Paul, A., Noone, D., Contreras-Rosales, A., and Thirumalai, K.: Orbitally driven evolution of Asian monsoon and stable water isotope ratios during the Holocene: Isotope-enabled climate model simulations and proxy data comparisons, Quaternary Science Reviews, 252, 106 743, 2021.

https://doi.org/10.5194/egusphere-2026-3894
Preprint. Discussion started: 28 July 2026

Tharammal, T., Bala, G., and Nusbaumer, J.: Drivers of the δ 18 O changes in Indian Summer Monsoon precipitation between the Last Glacial Maximum and pre-industrial period, Climate of the Past, 22, 427–444, 2026.

Tian, Y., Fleitmann, D., Zhang, Q., Sha, L., Wassenburg, J. A., Axelsson, J., Zhang, H., Li, X., Hu, J., Li, H., et al.: Holocene climate change in southern Oman deciphered by speleothem records and climate model simulations, Nature Communications, 14, 4718, 2023.

Wanner, H., Beer, J., Bütikofer, J., Crowley, T. J., Cubasch, U., Flückiger, J., Goosse, H., Grosjean, M., Joos, F., Kaplan, J. O., et al.: Mid-to Late Holocene climate change: an overview, Quaternary Science Reviews, 27, 1791–1828, 2008.

Werner, M., Langebroek, P. M., Carlsen, T., Herold, M., and Lohmann, G.: Stable water isotopes in the ECHAM5 general circulation model: Toward high-resolution isotope modeling on a global scale, Journal of Geophysical Research: Atmospheres, 116, 2011.

Winnick, M. J., Chamberlain, C. P., Caves, J. K., and Welker, J. M.: Quantifying the isotopic 'continental effect', Earth and Planetary Science Letters, 406, 123–133, 2014.

Zhang, J., Liang, M.-Q., Li, J.-Y., Wu, Y., Xue, Y.-X., Sun, W.-J., Liu, X.-Z., Chen, J.-K., Chen, C.-J., and Li, T.-Y.: Upstream moisture sources and circulation patterns controls Asian monsoon hydroclimate over the past 20,000 years, Quaternary Science Reviews, 363, 109 438, 2025.

https://doi.org/10.5194/egusphere-2026-3894
Preprint. Discussion started: 28 July 2026

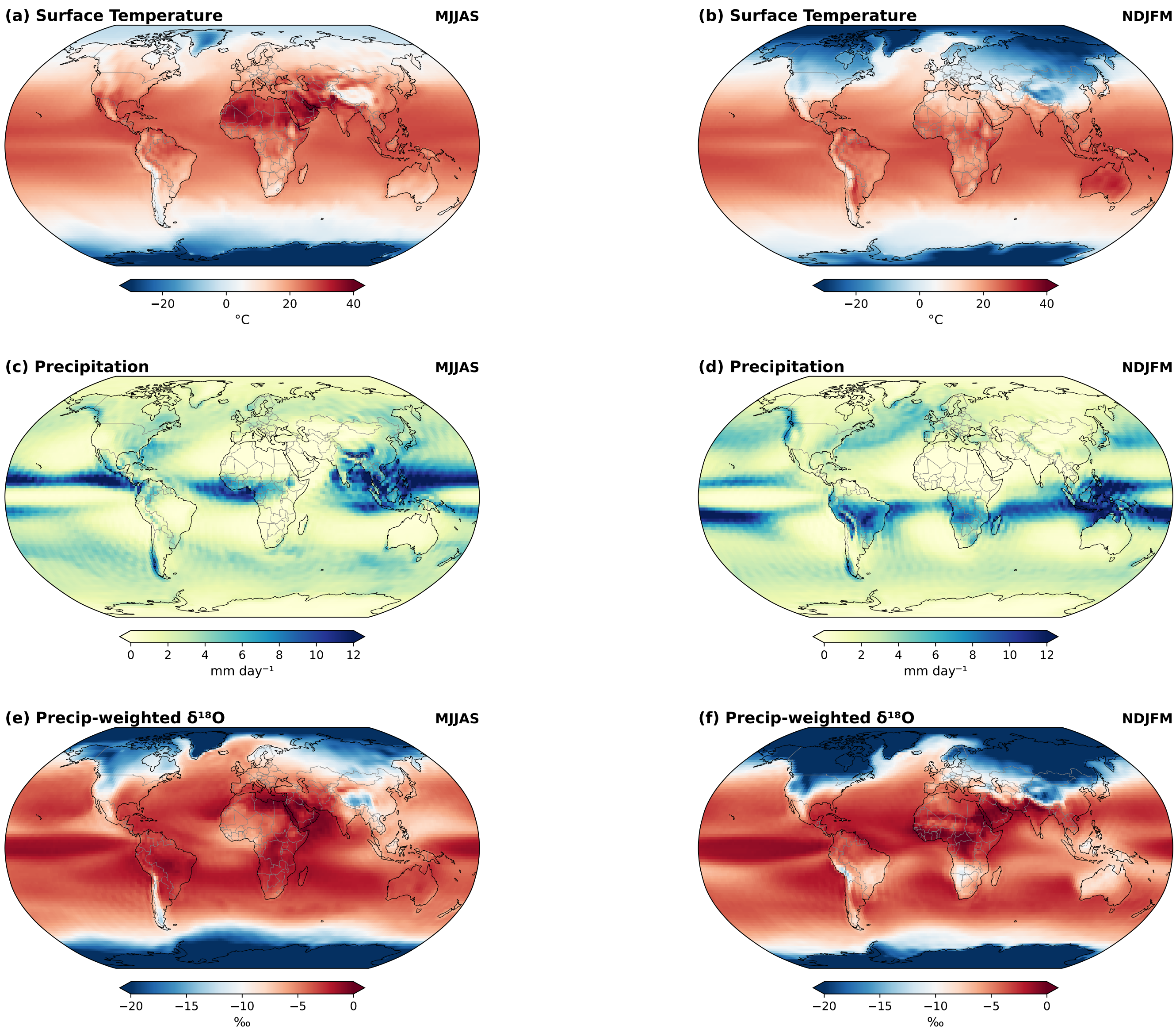

Figure 1. Pre-industrial (PI; last 500 yr of simulation) mean state of surface temperature (°C), precipitation (mm day^{-1}), and precipitation-weighted δ^{18}O (‰). Left column: MJJAS; right column: NDJFM.

https://doi.org/10.5194/egusphere-2026-3894
Preprint. Discussion started: 28 July 2026

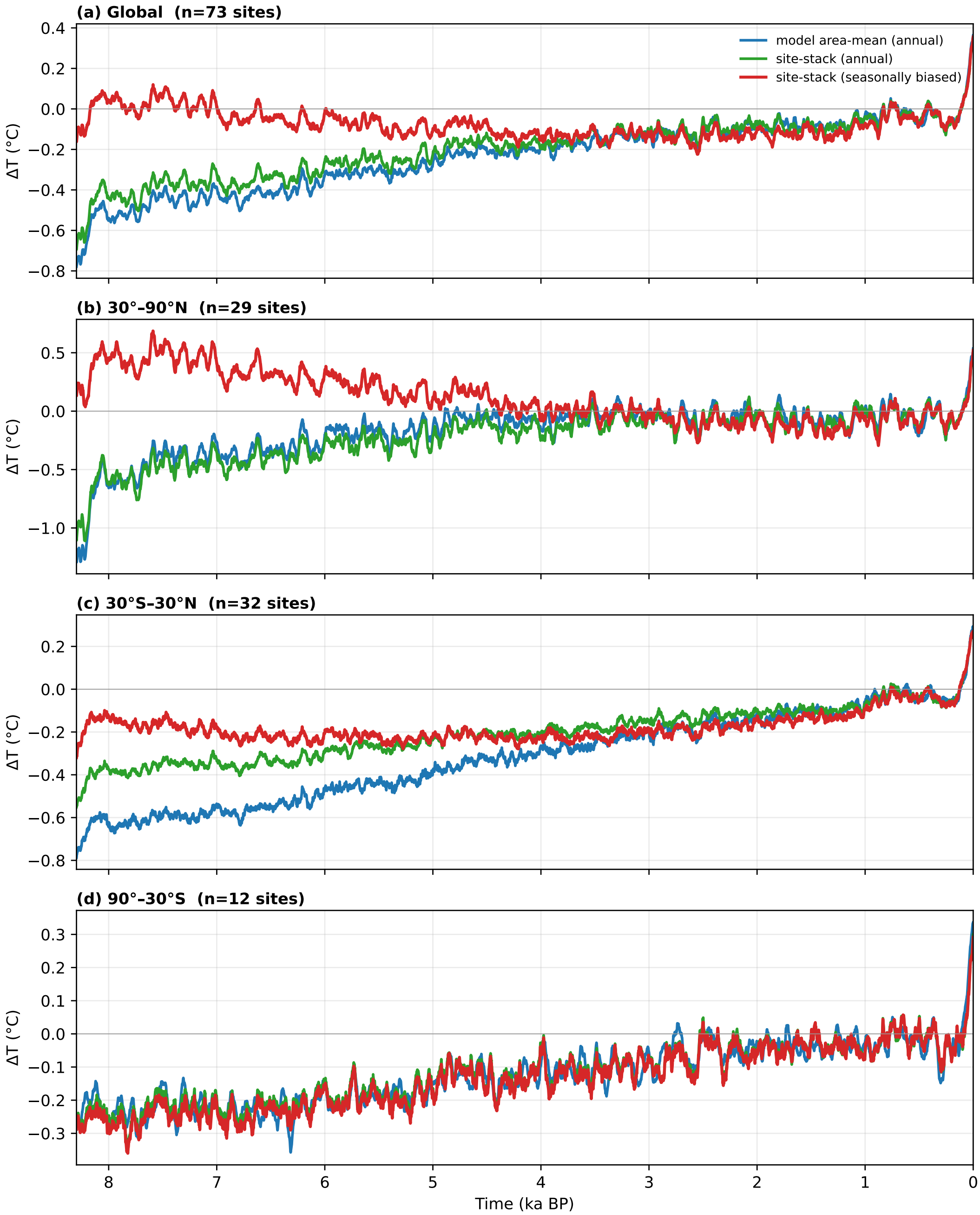

Figure 2. Simulated transient surface air temperature anomalies (°C) relative to the last 500 model years over the past 8300 years for (a) global mean, (b) northern extratropics (30°–90°N), (c) tropics (30°S–30°N), and (d) southern extratropics (90°–30°S). Blue lines show the model area-mean annual temperature averaged over each band, green lines show the site-stack using annual model output sampled at the Marcott et al. (2013) proxy sites, and red lines show the same site-stack with seasonal sampling applied at each site following the seasonality reported in the original Marcott database, with all Northern Hemisphere marine sites forced to boreal summer (JJA) as in Liu et al. (2014). The number of Marcott sites included in each band is given in the panel headers.

https://doi.org/10.5194/egusphere-2026-3894
Preprint. Discussion started: 28 July 2026

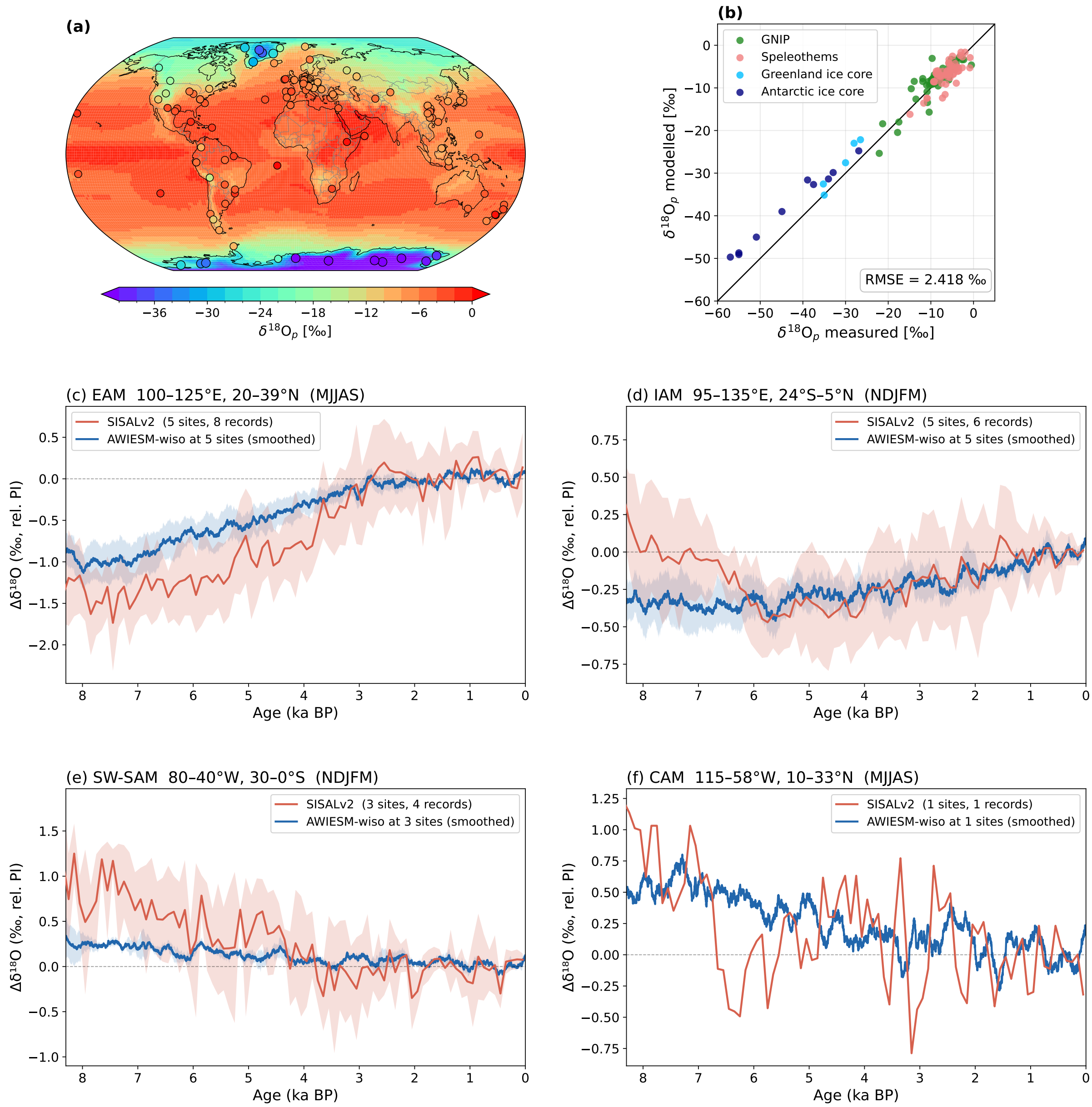

Figure 3. (a) Simulated pre-industrial (shading) and observed present-day (circles) precipitation-weighted annual mean δ^{18}O in precipitation. (b) Scatter plot of modelled versus measured $\delta^{18}O_p$. Observed values are based on the GNIP database, speleothems, and ice core records. (c–f) Holocene δ^{18}O anomalies (relative to the pre-industrial mean) for monsoon regions with continuous speleothem coverage spanning 8000 BP to present: East Asian Monsoon (EAM), Indo-Australian Monsoon (IAM), southwestern South American Monsoon (SW-SAM), and Central American Monsoon (CAM). Blue lines show AWIESM-wiso simulated precipitation-weighted δ^{18}O extracted at SISAL site locations (200-yr running mean); blue shading indicates $\pm1\sigma$ spread across model grid points. Red lines show the SISALv2 speleothem composite (median per entity per 100-yr bin, then mean across entities); red shading indicates $\pm1\sigma$ inter-entity spread. Only speleothem entities continuously covering 8000–500 BP are included. All anomalies are expressed relative to the 0–500 BP (pre-industrial) mean.

https://doi.org/10.5194/egusphere-2026-3894
Preprint. Discussion started: 28 July 2026

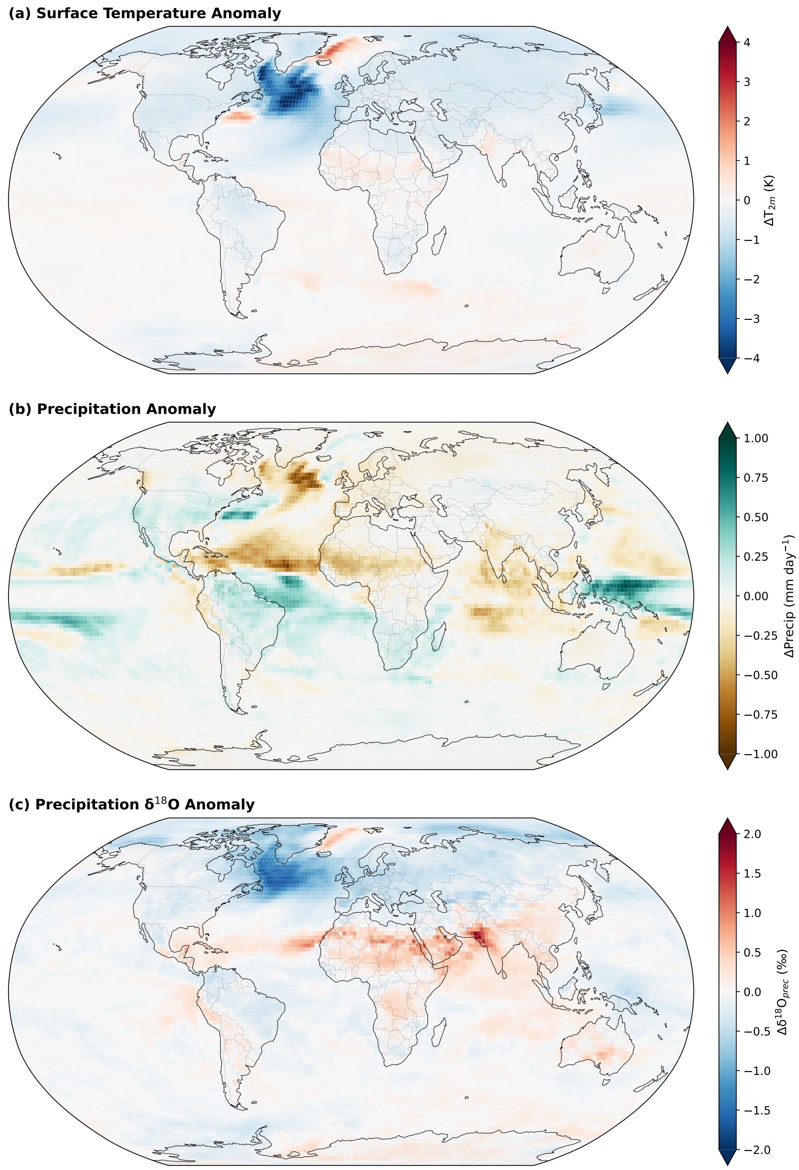

Figure 4. Simulated responses in annual mean surface temperature (°C kyr^{-1}), precipitation (mm day^{-1} kyr^{-1}), and precipitation-weighted δ^{18}O (‰ kyr^{-1}) to the 8.2 ka freshwater hosing.

https://doi.org/10.5194/egusphere-2026-3894
Preprint. Discussion started: 28 July 2026

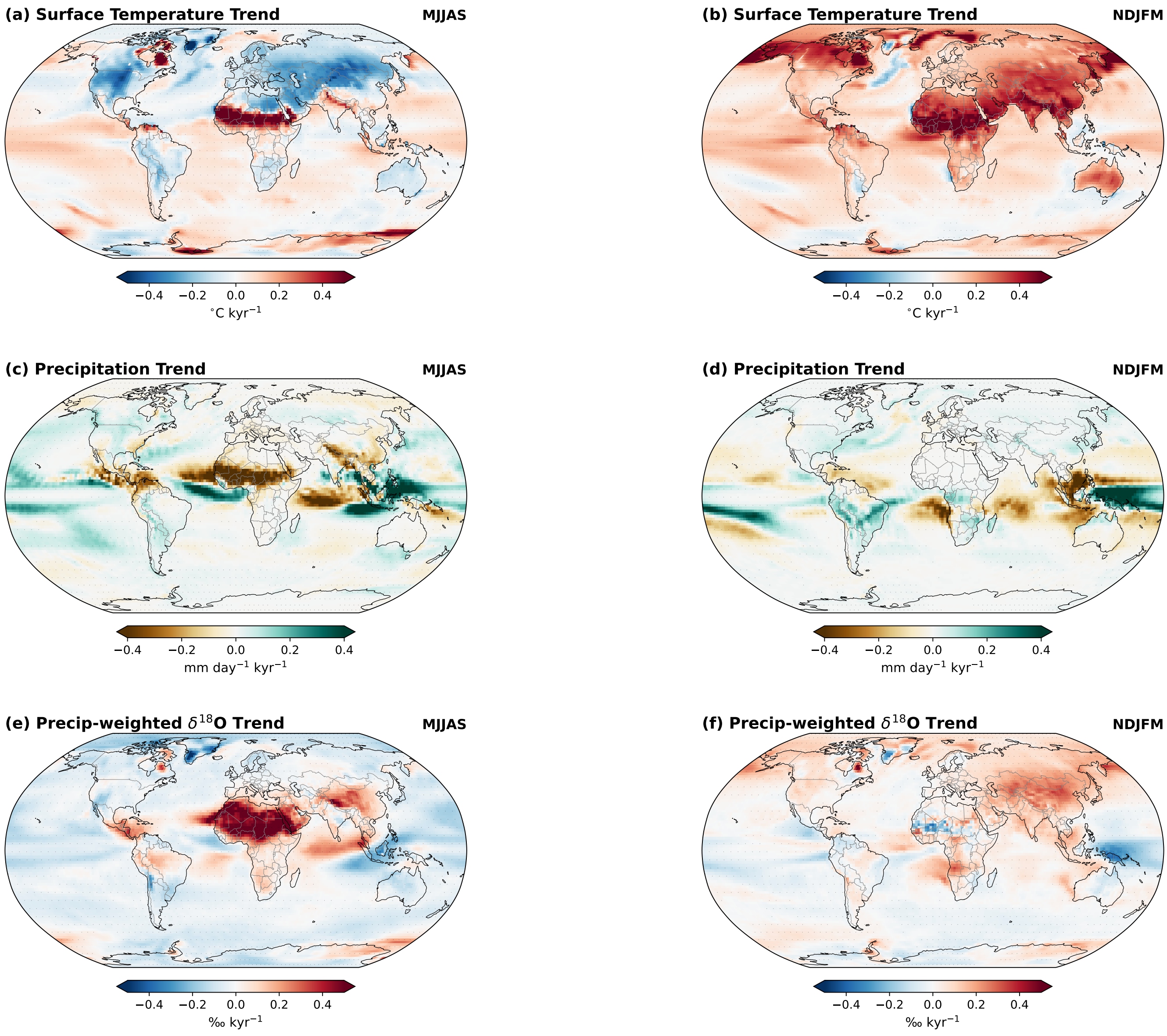

Figure 5. Linear trends in surface temperature (°C kyr^{-1}), seasonal precipitation (mm day^{-1} kyr^{-1}), and precipitation-weighted δ^{18}O (‰ kyr^{-1}) over the Holocene (8,200–0 yr BP) from the AWIESM-wiso transient simulation. Left column: MJJAS; right column: NDJFM. Stippling marks grid cells where the trend is significant at $p < 0.05$ (linear regression t-test).

https://doi.org/10.5194/egusphere-2026-3894
Preprint. Discussion started: 28 July 2026

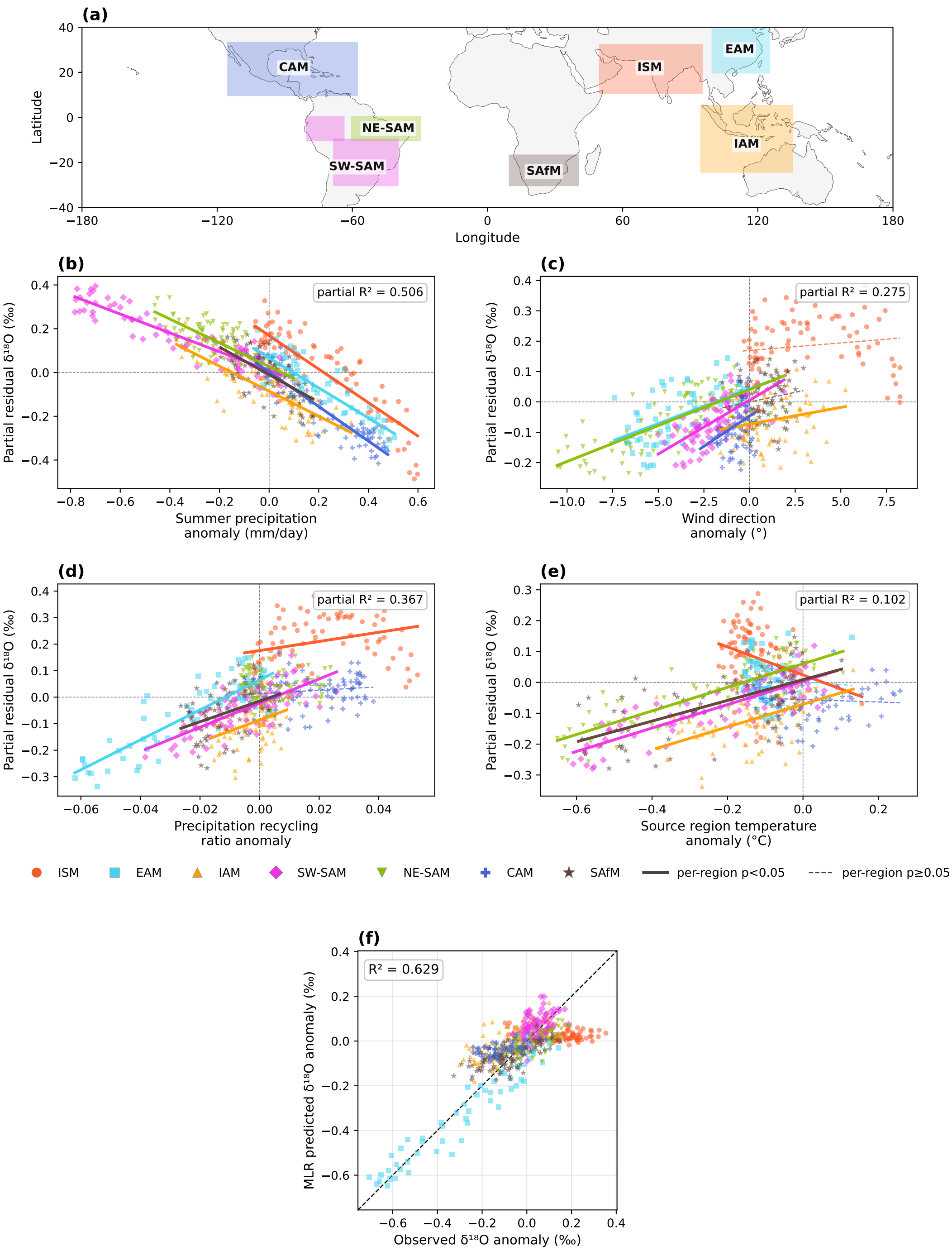

Figure 6. (a) Monsoon regions. (b–e) Partial-residual plots for the four-predictor MLR fitted to 100-yr binned anomalies pooled across seven monsoon regions (3σ outliers removed). Each panel shows the partial effect of one predictor on precipitation δ^{18}O after removing the linear influence of the other three. The pooled fit yields $R^2 = 0.629$. Coloured symbols mark individual regions; the black line shows the pooled slope. (f) Simulated versus MLR-predicted precipitation δ^{18}O anomalies for the 100-yr binned dataset (pooled across the seven monsoon regions). The dashed line marks the 1:1 reference; symbols are colour-coded by region.

https://doi.org/10.5194/egusphere-2026-3894
Preprint. Discussion started: 28 July 2026

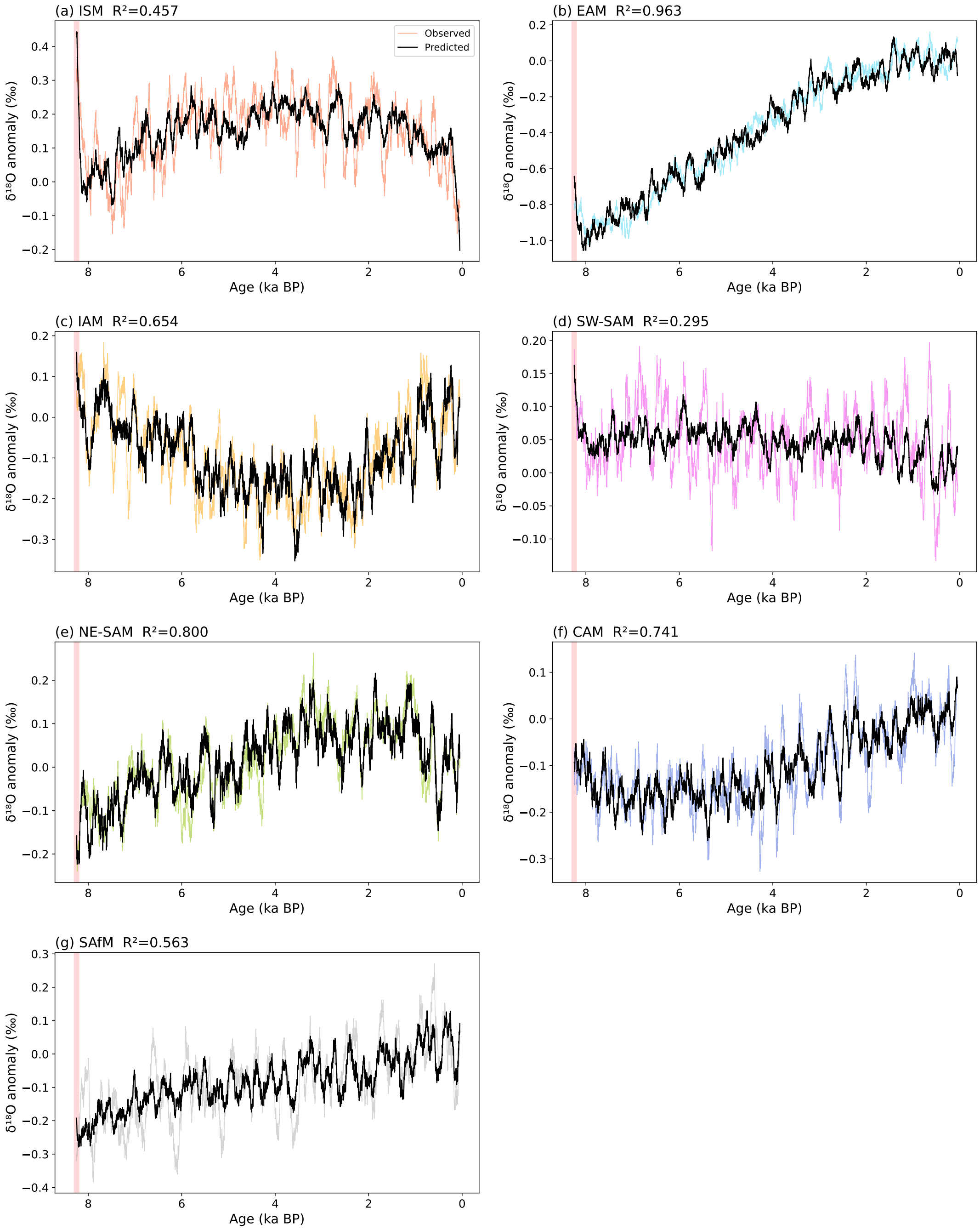

Figure 7. Observed (coloured) and MLR-predicted (black) precipitation δ^{18}O anomalies for each monsoon region, with the four-predictor model fitted directly on the 100-yr rolling-mean series with the long-term Holocene trend retained. The red bar at 8.3–8.2 ka marks the freshwater-hosing interval included in the simulation. Per-region R^2 values are quoted in the panel titles.

https://doi.org/10.5194/egusphere-2026-3894
Preprint. Discussion started: 28 July 2026

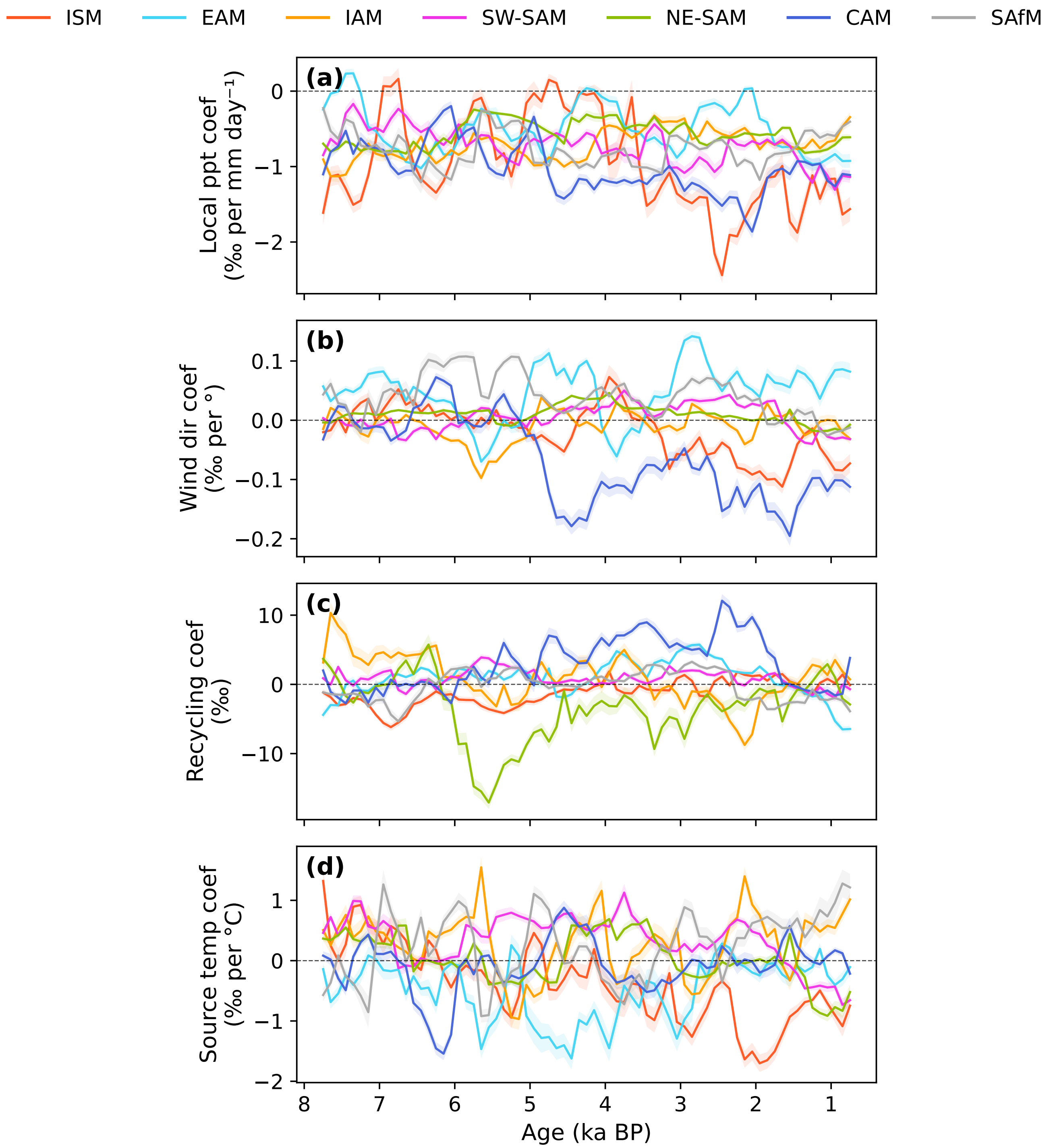

Figure 8. Rolling four-predictor MLR coefficients computed in a 1000-yr window stepped every 100 yr along the 8.3–0 ka transient, after applying a 100-yr rolling mean to the input series. Each panel shows one predictor coefficient as a function of time, with the seven monsoon regions colour-coded and the shading marking the 95 % confidence interval.

https://doi.org/10.5194/egusphere-2026-3894
Preprint. Discussion started: 28 July 2026

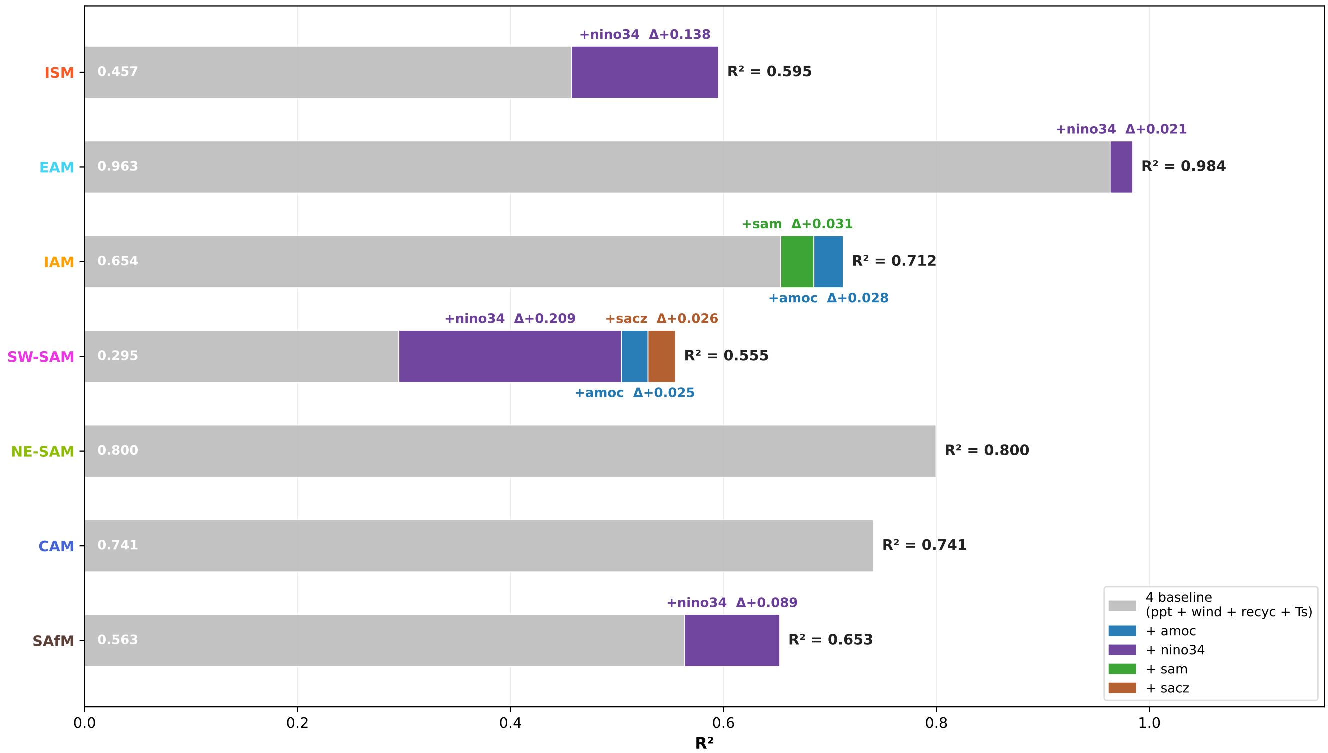

Figure 9. R^2 gain from adding up to two climate indices to the four-predictor baseline MLR for each of the seven monsoon regions. Grey bars show the baseline R^2 obtained with the standard predictor set (region precipitation, source wind direction, recycling ratio, source temperature). Colored segments show the incremental R^2 contribution of the climate index selected by forward stepwise search from the candidate pool (AMOC, Niño3.4, SAM, AO, SACZ strength, SACZ tilt), where an index is retained only if it raises R^2 by at least 0.02 over the previous step. Numbers in the grey blocks give baseline R^2; values to the right of each bar give the final R^2 after gated addition.

https://doi.org/10.5194/egusphere-2026-3894
Preprint. Discussion started: 28 July 2026

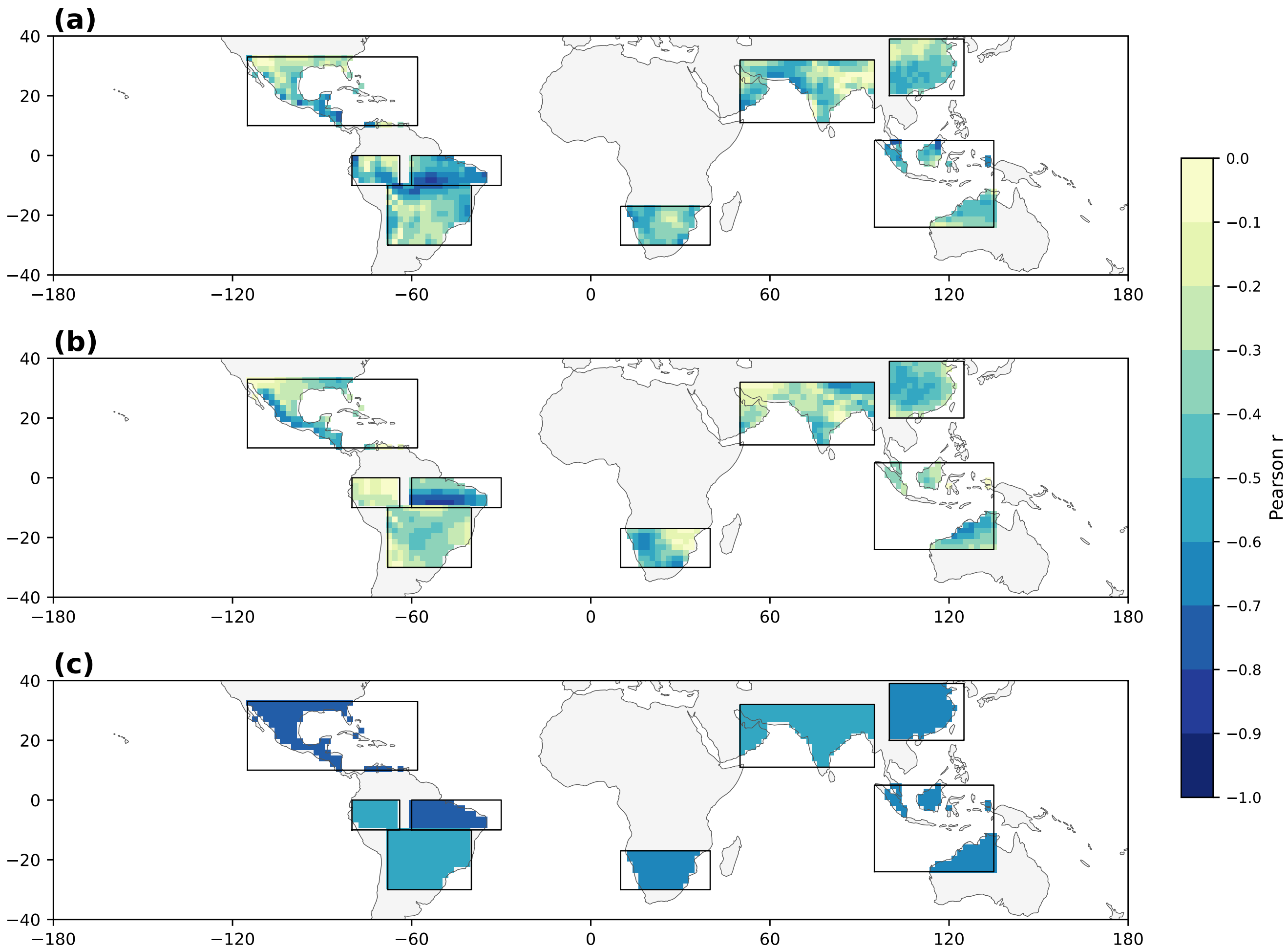

Figure 10. Pearson correlation between simulated precipitation δ^{18}O and precipitation inside the seven monsoon domains, computed on the seasonal mean appropriate to each region (MJJAS for NH, NDJFM for SH) over the full 8,199-yr base run. (a) Grid-cell δ^{18}O against grid-cell precipitation; (b) grid-cell δ^{18}O against the regional-mean precipitation; (c) regional-mean δ^{18}O against regional-mean precipitation, painted uniformly across the box. The colour scale spans the full range of observed correlations, all of which are negative.